

## Diffusion and conformational dynamics in locally perturbed model membrane systems

*Eugene P. Petrov\**, *Petra Schwille*<sup>#</sup>

Max Planck Institute of Biochemistry, Department of Cellular and Molecular Biophysics,  
Martinsried, Germany

\*petrov@biochem.mpg.de, #schwille@biochem.mpg.de

### Abstract

In this article, we review our results on diffusion and phase separation in lipid membranes, as well as on interaction of membranes with colloidal particles, biomacromolecules, and supramolecular assemblies, which were obtained within the framework of the Saxon Research Unit FOR 877 “From Local Constraints to Macroscopic Transport”.

Keywords: Cytoskeleton, diffusion, DNA, DNA origami, giant unilamellar vesicles, lipid membranes, membrane domains, Monte Carlo simulations, phase separation, polyelectrolyte

### 1 Introduction

The plasma membrane is an extremely important component of the living cell. It not only defines the boundaries of the organelles and the cell itself, it creates barriers between cell compartments and their environment. The membrane, however, does not merely serve as a passive barrier – it is characterized by a high functionality, as numerous processes vitally important for the cell take place at or across the membrane. Most of these processes are driven by diffusion in the membrane, and it is therefore important to be able to relate membrane diffusion to physical parameters of the membrane, surrounding media and diffusing particles. As a result of the two-dimensional geometry of the membrane, situations where diffusion is affected by particle crowding are easily achieved. The lipid membrane is typically characterized by a high bending flexibility, and therefore can adjust its local curvature in response to adhesion of a colloidal particle or a macromolecule, which can lead to membrane-mediated interaction of membrane-bound particles. Cell membranes consist of a number of lipids, and thus can exhibit different phases, phase coexistence, and critical behavior, which provides yet an additional type of membrane response to local perturbations by macromolecular structures, including the membrane cytoskeleton.

In this work we give an overview of the results of our research on topics we have just outlined, which were carried out within the framework of the Saxon Research Unit FOR 877 “From Local Constraints to Macroscopic Transport”. For a detailed presentation of the experimental protocols, numerical

approaches, and simulation techniques employed in our studies, as well as for an extended discussion of the relevant literature, an interested reader is kindly advised to look into our original papers.

## 2 Translational and rotational diffusion of membrane inclusions

Brownian motion in lipid membranes is distinguished from diffusion in homogeneous bulk media by a peculiar feature, which has first been discovered by Saffman and Delbrück in the beginning of 1970s. Namely, as a result of hydrodynamic interactions which are mediated by the fluids surrounding the membrane, an additional hydrodynamic length scale, known as the Saffman–Delbrück (SD) length  $l_{SD}$ , emerges. It is determined in terms of the surface viscosity of the membrane  $\eta$  and the bulk viscosities of the surrounding media  $\mu_1$  and  $\mu_2$ :  $l_{SD} = \eta/(\mu_1 + \mu_2)$ . As a result, the character of diffusion of a membrane inclusion depends on its reduced radius  $\varepsilon = a/l_{SD}$ : diffusion of small inclusions with  $\varepsilon \ll 1$  is controlled by the 2D membrane dynamics, while the motion of large inclusions with  $\varepsilon \gg 1$  is determined by the bulk 3D dynamics of the surrounding fluids.

The simple approximate expression originally developed by Saffman and Delbrück to describe behavior of membrane proteins cannot be applied to analyze data on diffusion of larger inclusions. The exact hydrodynamics-based solution of this problem has been developed by Hughes, Pailthorpe, and White (HPW) in the early 1980s. The exact HPW solution, however, cannot be presented in a closed form, and even its numerical evaluation within the whole range of reduced sizes of membrane inclusions is a serious challenge. To provide a practical way of analyzing membrane diffusion data, we have developed an approach to stable numerical evaluation of the exact HPW solution [1] and constructed simple high-accuracy analytical approximations to the exact HPW solutions for the translational and rotational diffusion coefficients of membrane inclusions using the analytical matching of small- $\varepsilon$  and large- $\varepsilon$  asymptotics and numerical matching of the cross-over regime against the numerically evaluated exact HPW solution [1, 2].

We present the translational and rotational diffusion coefficients in the following form:  $D_T(\varepsilon) = D_{T0}\Delta_T(\varepsilon)$ ,  $D_R(\varepsilon) = D_{R0}\Delta_R(\varepsilon)$ , where  $D_{T0} = k_B T/(4\pi\eta)$  and  $D_{R0} = k_B T(\mu_1 + \mu_2)^2/(4\pi\eta^3)$ . The dimensionless reduced translational and rotational mobilities  $\Delta_{T,R}(\varepsilon)$  (Figure 1) are given as follows:

$$\Delta_T(\varepsilon) = [\ln(2/\varepsilon) - \gamma + 4\varepsilon/\pi - (\varepsilon^2/2) \ln(2/\varepsilon)][1 - (\varepsilon^3/\pi) \ln(2/\varepsilon) + \beta(\varepsilon, b_{T1}, b_{T2}, c_{T1}, c_{T2})]^{-1} \quad (1)$$

$$\Delta_R(\varepsilon) = [\varepsilon^2 + 4\varepsilon^3/(3\pi) + \beta(\varepsilon, b_{R1}, b_{R2}, c_{R1}, c_{R2})]^{-1}, \quad (2)$$

where  $\gamma = 0.577215\dots$  is the Euler constant, and  $\beta(\varepsilon, p, q, v, w) = v\varepsilon^p/(1 + w\varepsilon^q)$  is a bridging function, which provides proper cross-over from the analytically matched small- $\varepsilon$  and large- $\varepsilon$  asymptotics. The numerical coefficients providing the best agreement with the numerical results are [1, 2]:  $b_{T1} = 2.74819$ ,  $b_{T2} = 0.51465$ ,  $c_{T1} = 0.73761$ ,  $c_{T2} = 0.52119$ ;  $b_{R1} = 2.91587$ ,  $b_{R2} = 0.68319$ ,  $c_{R1} = 0.31943$ ,  $c_{R2} = 0.60737$ .

Using this approach, we were able to successfully analyze experimental data on translational diffusion of  $L_d$  domains in the  $L_o$  phase of DOPC/DPPC/Chol membranes to correctly determine the thermal activation energy for the  $L_o$  phase of this lipid composition [1]. The use of our expression allowed us to successfully determine the surface viscosity of freestanding DOPC membrane from measured

diffusion coefficients of membrane-bound polystyrene beads with radii of 10, 20, and 50 nm ( $\eta_{\text{DOTAP}} \approx 6 \cdot 10^{-10}$  Pa·s·m) [6], as well as to estimate the dimensions of DNA globules on cationic lipid membranes (see below).

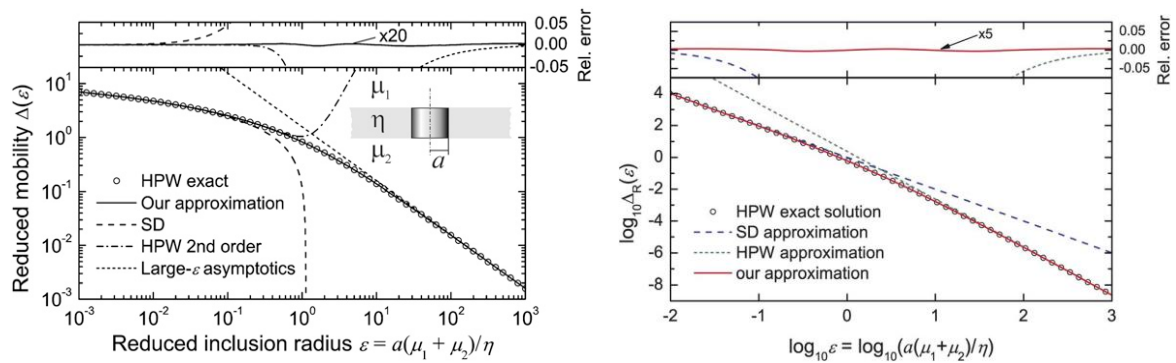


Figure 1: (left) Reduced translational mobility of an inclusion in a membrane inclusion: the exact HPW result, SD approximation (dashed curve), HPW second-order approximation (dash-dotted curve), the large- $\varepsilon$  asymptotics (dotted line), and the approximation proposed by the authors (solid curve). All curves are computed under the assumption of the no-slip condition at the inclusion boundary. The upper subpanel shows the relative errors of the corresponding approximations. (From Ref. [1]. Copyright © by The Biophysical Society, 2008.) (right) Reduced rotational mobility of a membrane inclusion: the exact HPW result (circles), SD approximation (dashed line), HPW large- $\varepsilon$  asymptotics (dotted line), and the approximation proposed by the authors (solid curve). The upper panel shows the relative errors of the corresponding approximations. (From Ref. [2]. Copyright © by The Royal Society of Chemistry (RSC), 2012.)

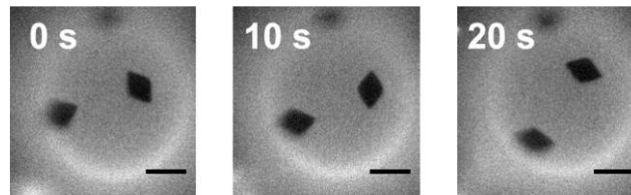


Figure 2: Fluorescence microscopy images of the upper pole area of a giant unilamellar vesicle with diamond-shaped gel-phase domains (dark) recorded consecutively every 10 s. Vesicle radius  $R_{\text{GUV}} = 20 \mu\text{m}$ . Membrane composition: DPhPC/DPPC 50:50. Temperature:  $23.5 \pm 1 \text{ }^\circ\text{C}$ . Scale bar:  $5 \mu\text{m}$ . (From Ref. [2]. Copyright © by The Royal Society of Chemistry (RSC), 2012.)

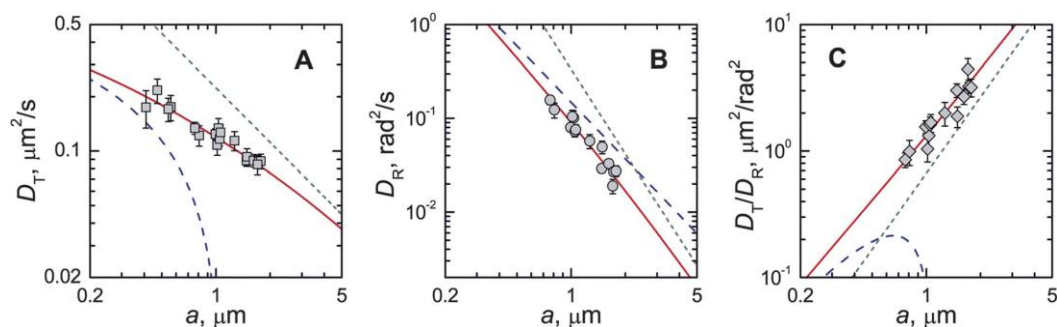


Figure 3: Translational ( $D_T$ ) (A) and rotational ( $D_R$ ) (B) diffusion coefficients of diamond-shaped gel-phase domains in DPhPC/DPPC giant unilamellar vesicles and their ratio  $D_T/D_R$  (C). Solid lines in panels (A) and (B) show the global weighted least-squares fit of translational and rotational data using Eqs. (1) and (3). The dashed and dotted lines show the small-size (SD approximation) and large-size asymptotic dependences. Lines in panel (C) represent ratios of the corresponding model predictions shown in panels (A) and (B). Because of a limited time resolution, rotational diffusion coefficients could be determined only for domains with the effective radius  $a > 0.7 \mu\text{m}$ . Membrane composition: DPhPC/DPPC 50:50. Temperature:  $23.5 \pm 1 \text{ }^\circ\text{C}$ . (From Ref. [2]. Copyright © by The Royal Society of Chemistry (RSC), 2012.)

Further, we demonstrated the power of the approach by simultaneous analysis of data on translational and rotational diffusion of gel-phase domains surrounded by the liquid-disordered membrane phase [2]. In these experiments, we used membranes with the composition DPhPC/DPPE 50:50, for which gel-phase domains with a remarkable diamond shape are formed (Figure 2). This domain shape, which has never been reported in the literature previously, allowed us to easily track both their positions and orientations, and obtain data on the translational and rotational diffusion coefficients which can be successfully described using one and the same value of the membrane surface viscosity  $\eta \approx 2.2 \cdot 10^{-9}$  Pa·s·m (Figure 3).

### 3 Diffusion dynamics of membrane-bound rodlike DNA origami particles in dilute and concentrated regime

The recent break-through in DNA nanotechnology made it possible to carry out nanoscale folding of DNA into custom-shaped objects known as DNA origami. The DNA origami approach allows one to construct 2D and 3D nano-objects with pre-designed structure and rigidity. Another crucial feature of this technology is the possibility of selective functionalization of the resulting structures with nanometer precision. In our work [3, 4] we used DNA origami in the form of stiff needle-like six-helix bundles (contour length 420 nm, diameter 6 nm, persistence length 1.8  $\mu$ m) which were additionally modified by adding two or eight cholesterol anchors to provide their binding to a lipid membrane (Figure 4).

Using Fluorescence Correlation Spectroscopy (FCS) to observe the dynamics of DNA origami nanoneedles bound to a freestanding membrane mimicked by GUVs made of DOPC, we have demonstrated [3] that position-selective fluorescent labeling of DNA origami nanoneedles at the center and the end of the structure allows one to reliably determine their translational and rotational diffusion coefficients (Figure 5a). The fact that diffusion coefficients  $D_T$  and  $D_R$  in the dilute regime depend on the number of membrane anchors, and that additionally, even in case of eight membrane anchors they are factor of  $\sim 1.5$  larger than the prediction of the hydrodynamics-based theory for needle-like membrane inclusion, allowed us to conclude that the nanoneedles just glide over the membrane surface, being held by the anchors buried in the bilayer.

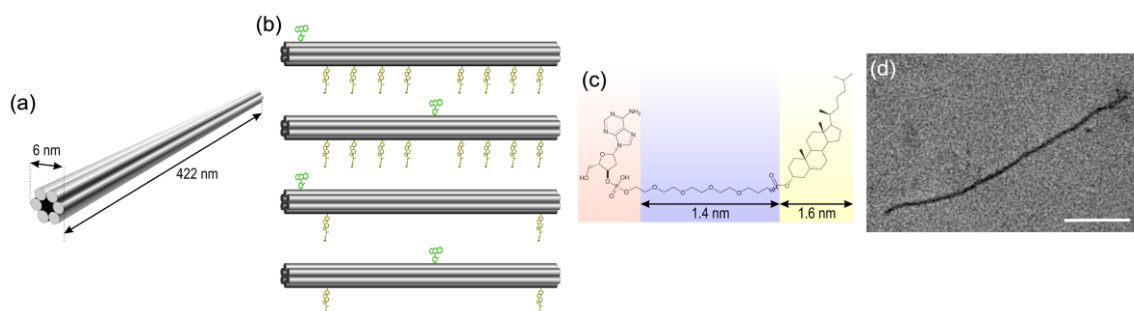


Figure 4: Cholesteryl-triethylene glycol-anchored DNA origami nanoneedles. Schematics of six-helix bundles (a) with eight and two membrane anchors and a fluorescent label at one of the ends or at the center of mass (b). (c) Detailed structure of a cholesteryl-triethylene glycol-modified nucleotide used to produce the membrane anchors. (d) Representative transmission electron microscopy image of a DNA origami nanorod (scale bar: 100 nm). (From Ref. [4]. Copyright © by The American Chemical Society, 2015.)

As a result of steric interactions, dynamics of a 2D system of hard needle-like objects depends on the surface density of particles. According to the theory, an isotropic-nematic (IN) transition is expected to take place when the needles reach the reduced surface density  $\rho = \sigma L^2 \approx 7$ , where  $\sigma$  is the surface density and  $L$  is the length of the needle. Apart from its basic importance in the context of behavior of colloidal and granular matter, the IN transition of strongly elongated particles in 2D can also have a fundamental biological relevance – in particular, in processes of membrane shape transformation by strongly elongated proteins from the BAR domain superfamily, reticulons and caveolin. In spite of the importance of the problem, both theoretical and experimental results on diffusion dynamics in 2D ensembles of hard needle-like particles were missing before publication of our work [4].

To study the IN transition, we carried out FCS measurements on ensembles of DNA origami nanoneedles bound to freestanding lipid membranes as a function of the surface density of particles. To ensure that only self-diffusion contributes to the data, a signal from a tiny fraction of nanoneedles was detected using specific fluorescence labeling (for details, see the original work). The results were compared with Monte Carlo simulations of Brownian hard needles in 2D covering a similar range of particle surface densities. Both translational and rotational diffusion were found to be strongly suppressed with an increase in the surface density of the nanoneedles (Figures 5b, 6) and show a remarkable agreement with the results of simulations. The results agree with the theory which predicts that the IN transition in a hard needle ensemble should take place at  $\rho = \sigma L^2 \approx 7$ . This indicates that in our experiments we clearly observe the onset of the IN transition in 2D. The remarkable agreement of the experimental results with the outcome of simulations based on an extremely simple model indicates that under the given experimental conditions the IN transition is induced by the direct steric interaction of DNA origami nanoneedles.

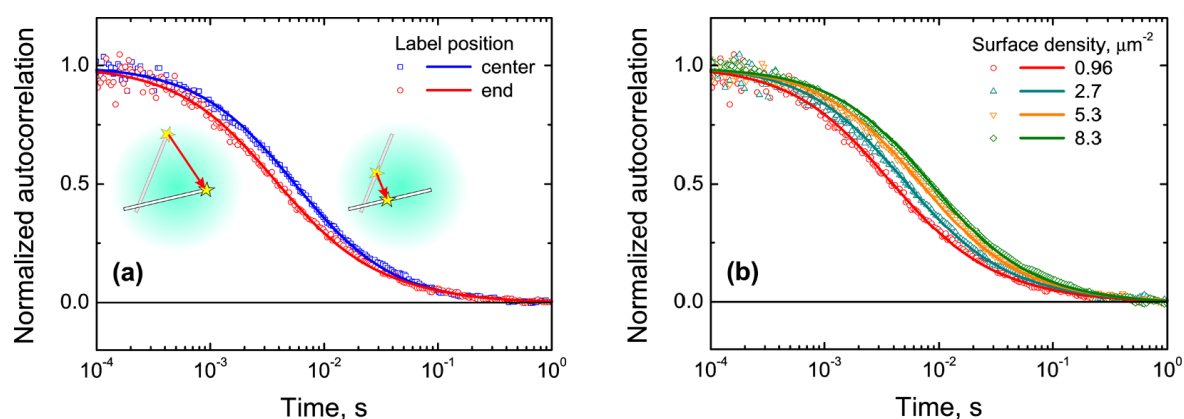


Figure 5: Diffusion dynamics of DNA origami nanoneedles bound to a freestanding lipid membrane as detected by FCS. Representative FCS autocorrelation curves for membrane-bound nanoneedles with eight membrane anchors fluorescently labeled at the center of mass or at one of the ends (symbols) along with their fits using the model described in the text (solid curves). (a) Effect of the label position at a low surface density of nanoneedles: ( $\square$ ) center-labeled,  $\sigma = 0.82 \mu\text{m}^{-2}$  ( $\rho = 0.15$ ) and ( $\circ$ ) end-labeled,  $\sigma = 0.96 \mu\text{m}^{-2}$  ( $\rho = 0.17$ ). The graphical insets illustrate the effect of the fluorescent label position on the character of fluorescence fluctuations for a particle moving in a Gaussian detection spot. (b) Effect of the surface density for end-labeled nanoneedles: ( $\circ$ )  $\sigma = 0.96 \mu\text{m}^{-2}$  ( $\rho = 0.17$ ), ( $\Delta$ )  $\sigma = 2.7 \mu\text{m}^{-2}$  ( $\rho = 0.48$ ), ( $\nabla$ )  $\sigma = 5.3 \mu\text{m}^{-2}$  ( $\rho = 0.94$ ), and ( $\diamond$ )  $\sigma = 8.3 \mu\text{m}^{-2}$  ( $\rho = 1.46$ ). The number of fluorescent particles in the detection volume of the green (red) channel in these measurements was 0.11 (0), 0.31 (0), 0.09 (0.84), and 0.07 (1.41), respectively. (From Ref. [4]. Copyright © by The American Chemical Society, 2015.)

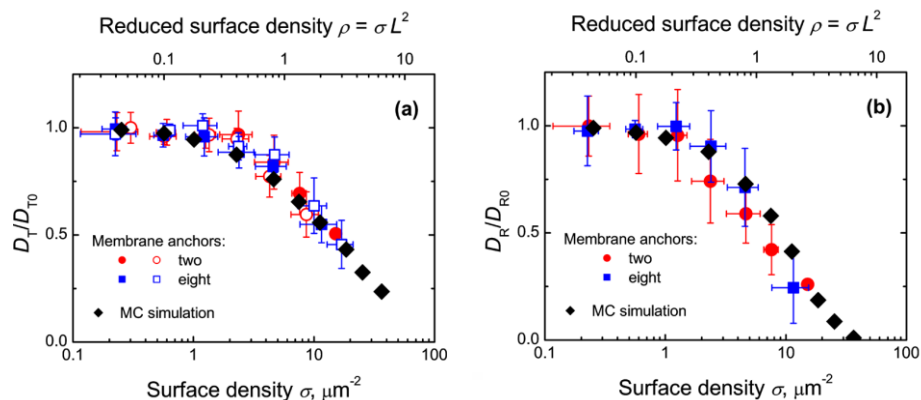


Figure 6: Reduced translational (a) and rotational (b) diffusion coefficients as a function of the surface density of DNA origami nanoneedles attached to the membrane with two ( $\circ$ ,  $\bullet$ ) and eight ( $\square$ ,  $\blacksquare$ ) membrane anchors (as determined from FCS data) and for Brownian hard needles in 2D (as determined from Monte Carlo simulations) ( $\blacklozenge$ ). Open and filled symbols representing experimental data denote results obtained for center- and end-labeled nanoneedles, respectively. (From Ref. [4]. Copyright © by The American Chemical Society, 2015.)

#### 4 Behavior of semiflexible polymers tightly bound to a freestanding membrane.

##### Phenomenon of membrane-induced DNA condensation

Behavior of polyelectrolyte molecules of various stiffness adsorbed on oppositely charged lipid membranes is an important problem of soft matter physics, which can give insight into molecular mechanisms of interaction of biomacromolecules with membranes of living cells. DNA is a perfect model polymer for these studies: it is negatively charged, its mechanical properties are well known and understood, its length and structure can be precisely controlled and, last but not least, DNA can be easily fluorescently labeled facilitating single-molecule microscopy experiments. These features were used in our experiments on interaction of DNA molecules with freestanding cationic lipid bilayers. Giant unilamellar vesicles represent a perfect experimental model system which mimics a freestanding lipid bilayer and can be used as an experimental platform to study interaction of polyelectrolytes with freestanding lipid membranes. The standard approach to GUV production by electroformation typically restricts the vesicle diameter to 20–40  $\mu\text{m}$ ; furthermore, GUVs may not be strongly attached to the substrate, which can considerably complicate experiments based on tracking membrane-bound particles. We have developed an experimental protocol [5] that allows one to overcome these difficulties and to reliably produce lipid structures which are fully suitable for the above experimental purposes. By following this protocol, one can reliably produce dome-shaped supergiant (diameter  $> 100 \mu\text{m}$ ) unilamellar vesicles (SGUVs) containing cationic lipids (Figure 7 left) by electroformation on ITO-coated electrodes. Because of their strong attachment to the substrate, these structures do not move laterally; furthermore, the combination of the large size of SGUVs allows for wide-field microscopy observations of the area exceeding  $\sim 300 \mu\text{m}^2$  of essentially flat freestanding membrane (Figure 7 right). Thus, cationic SGUVs represent a perfect experimental platform to study interaction of negatively charged polymers and colloids with freestanding membranes, which was used in our experiments on interaction of DNA macromolecules with freestanding cationic lipid membranes.

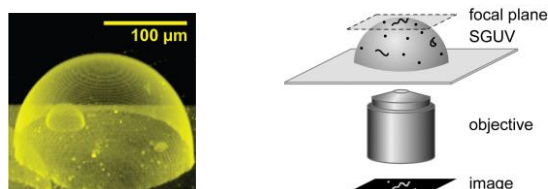


Figure 7: (left) Three-dimensional image of a supergiant unilamellar vesicle, SGUV, (DOPC/DOTAP 95:5) formed on the surface of an ITO-coated coverslip using electroformation. The 3D image is reconstructed from a set (Z-stack) of laser scanning microscopy images. (From Ref. [5]. Copyright © by The American Chemical Society, 2012.) (right) Schematic drawing of the fluorescence image acquisition of DNA adsorbed to the upper pole of a supergiant unilamellar vesicle that mimics a freestanding lipid bilayer (not to scale).

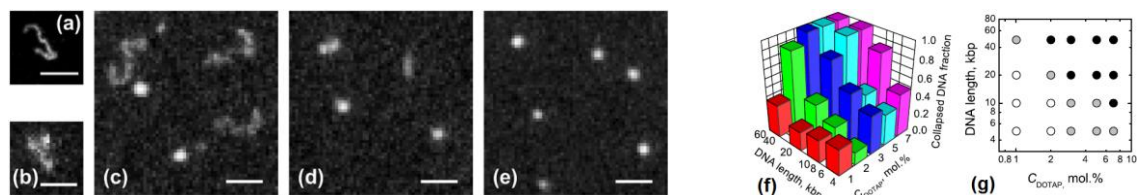


Figure 8: Fluorescence microscopy images of DNA molecules: (a) adsorbed on a supported fluid cationic lipid bilayer, (b) free in water surrounding cationic GUVs, (c)–(e) adsorbed on a freestanding fluid cationic lipid bilayer (GUV). DNA globules are visible as bright dots. DNA contour length: 48.5 kbp. Bilayer composition: DOPC/DOTAP.  $C_{\text{DOTAP}} = 10$  (a), 1 (c), 2 (d), and 7 mol% (e). Bar: 5  $\mu\text{m}$ . (f, g) Phase diagram for the coil-globule transition of DNA molecules at freestanding cationic lipid (DOPC/DOTAP) bilayers. In the right-hand panel, the fraction of condensed DNA is encoded by the shading of symbols: 0–0.35 (white), 0.35–0.65 (gray), and 0.65–1.0 (black). (From Ref. [6]. Copyright © by The American Physical Society, 2010.)

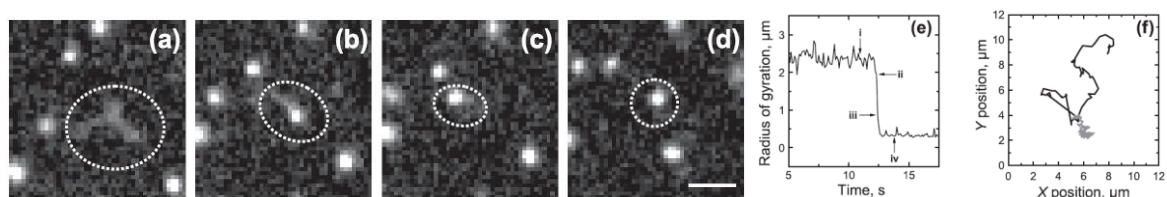


Figure 9: (a)–(d) Fluorescence microscopy images showing the collapse of a DNA molecule bound to a freestanding cationic lipid membrane. (a)  $t = 10.9$  s, (b)  $t = 12.3$  s, (c)  $t = 12.4$  s, (d)  $t = 13.8$  s. (e) Time dependence of the two-dimensional radius of gyration of the DNA molecule; arrows i, ii, iii, and iv correspond to images (a)–(d). (f) Brownian motion trajectory of the DNA molecule before (gray) and after (black) the collapse. DNA contour length 48.5 kbp. Bilayer composition: DOPC/DOTAP.  $C_{\text{DOTAP}} = 10$  mol%. Bar: 5  $\mu\text{m}$ . (From Ref. [6]. Copyright © by The American Physical Society, 2010.)

In our experiments on interaction of DNA macromolecules with freestanding cationic lipid membranes [6], SGUVs with the membrane in the fluid phase were produced from mixtures of zwitterionic lipid DOPC and cationic lipid DOTAP. Double-stranded DNA fragments with the lengths of 5, 10, 20, and 48.5 kbp ( $\lambda$ -DNA) were fluorescently stained using the YOYO-1 dye.

We have found that the conformation of DNA macromolecules adsorbed at cationic lipid bilayers strongly depended on the surface charge density of the membrane (Figure 8): whereas at low charge densities the macromolecules predominantly assumed the 2D random coil conformation, an gradual increase in the membrane charge lead to appearance of DNA molecules partially and eventually fully collapsed to form a compact globule with a size of order of the optical resolution of the microscope. Importantly, under the experimental conditions, the DNA globules are neither observed on supported lipid bilayer nor in solution. Rather, they are formed only after attachment of a DNA molecule to the freestanding cationic membrane, as has been documented in our single-molecule observations of

membrane-mediated DNA condensation (Figure 9). Thus formed DNA globules stay attached to the membrane and perform the translational Brownian motion.

By tracking and analyzing the Brownian trajectories of the DNA globules we have found (Figure 10) that the size of the DNA globules is virtually independent of the contour length of the DNA, but decreases rather strongly with an increase in the membrane charge density (from 250–350 nm for  $C_{\text{DOTAP}} = 1$  mol% to 130–200 nm for  $C_{\text{DOTAP}} = 7$  mol%).

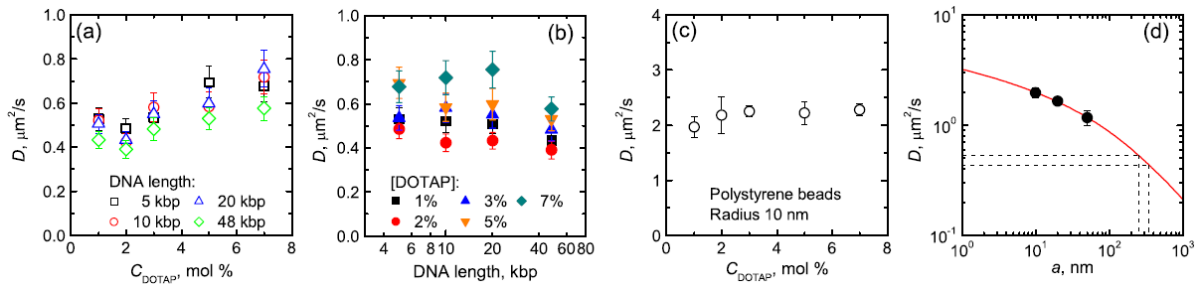


Figure 10: (a), (b) Translational diffusion coefficient of DNA globules bound to DOPC/DOTAP GUVs as a function of concentration of the cationic lipid (a) and DNA length (b). (a) DNA length 5 (□), 10 (○), 20 (Δ), and 48.5 kbp (◇). (b)  $C_{\text{DOTAP}} = 1$  (■), 2 (●), 3 (▲), 5 (▼), and 7 mol% (◆). (c), (d) Translational diffusion coefficient of membrane-bound 10-nm radius polystyrene beads as a function of concentration of the cationic lipid (c) and bead radius (d) ( $C_{\text{DOTAP}} = 1$  mol%). Panel (d) additionally shows the data fit using the model from Ref. [1] and an estimate for the DNA globule size at  $C_{\text{DOTAP}} = 1$  mol% (see text for details). (From Ref. [6]. Copyright © by The American Physical Society, 2010.)

On the other hand, we have found that electrostatic attachment of DNA macromolecules to gel-state freestanding membranes, which are characterized by a substantially higher viscosity and bending rigidity, does not lead to formation of DNA globules [7].

These experimental observations lead to a conclusion that the membrane-mediated DNA collapse involves strong local deformations of the membrane, which may provide the driving force for the membrane-driven compaction of the adsorbed macromolecule.

To gain a more quantitative understanding of the phenomenon, we have developed a model for membrane-driven DNA collapse [8]. The model assumes that membrane-driven compaction of an electrostatically adsorbed DNA leads to formation of a 2D flat “pancake” or “snail” globule. It is formed by wrapping around a spontaneously produced circular nucleus with an inner radius  $R_0$  or order of the DNA persistence length (provisionally taken to be  $\sim 500$  Å) (Figure 11). The model assumes that the membrane wraps around the oppositely charged DNA. This leads to local deformations of the membrane, which are favored by the electrostatic attraction and opposed by the bending energy of the membrane.

As a result, we found that for very reasonable combinations the parameters, including the strength of the electrostatic interaction (Debye screening length, local charge density in the membrane), membrane bending elasticity, and membrane tension, the model predicts appearance of membrane-mediated attraction between DNA segments and thus membrane-driven DNA compaction (Figure 12). The optimum DNA–DNA separation predicted by the model leads to size estimates of 2D snail globules which are in a very good agreement with our experimental observations [6].

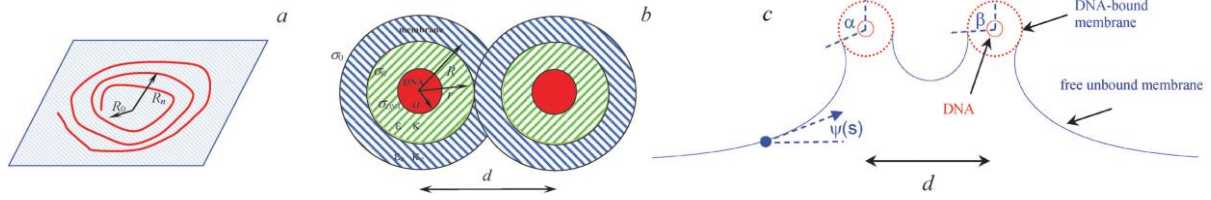


Figure 11: (a) Schematic representation of the 2D “snail” model of DNA condensation on a freestanding cationic lipid membrane. The cylindrical cell model (b) represents the cross-section of a one-layer-thick DNA snail shown in (a). The cationic membrane is in blue, the anionic DNA is in red, and the aqueous solution between them is in green. (c) Geometry of membrane wrapping around DNA rods as predicted by the model (the cross-section is shown). Straight DNA cylinders (red) are deposited on the same side of the membrane (blue). The corresponding wrapping angles  $\alpha$  and  $\beta$  are indicated. The tangent angle  $\psi(s)$  along the membrane contour is continuous. The dotted circles indicate the centerline of the membrane wrapping the DNAs, and the solid rings show the DNA cross-section. (From Ref. [8]. Copyright © by the PCCP Owner Societies, 2014.)

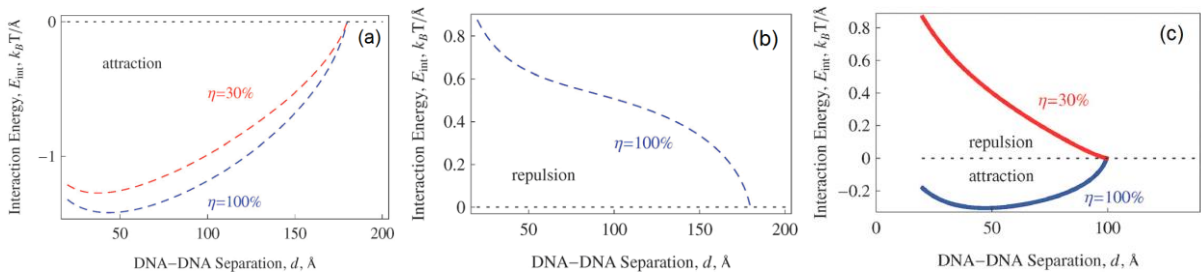


Figure 12: DNA–DNA membrane-mediated interaction is controlled by the local density of cationic lipids in the membrane  $\eta$ , Debye screening length  $1/\kappa_D$ , membrane bending rigidity  $\kappa$ , and membrane surface tension  $\sigma$ . (a)  $1/\kappa_D = 100 \text{ \AA}$ ,  $\kappa = 20 k_B T$ ,  $\sigma = 3 \text{ mN/m}$ ; (b)  $1/\kappa_D = 30 \text{ \AA}$ ,  $\kappa = 20 k_B T$ ,  $\sigma = 3 \text{ mN/m}$ ; (c)  $1/\kappa_D = 30 \text{ \AA}$ ,  $\kappa = 20 k_B T$ ,  $\sigma = 10 \text{ mN/m}$ . (From Ref. [8]. Copyright © by the PCCP Owner Societies, 2014.)

Interestingly, the model [8] predicts that under typical experimental conditions the membrane-driven attraction can be strong enough to induce collapse of rather stiff rodlike polymers electrostatically adsorbed to an oppositely charged freestanding membrane. Our recent experiments with much stiffer *fd*-virus particles (persistence length  $\sim 2 \mu\text{m}$ ) on freestanding cationic lipid membranes [9, 10] show that this indeed may well be the case.

## 5 Lattice-based Monte Carlo simulations of lipid membranes on experimentally relevant scales and time intervals

Motivated by the phenomenon of phase coexistence in multicomponent lipid membranes and its potential link with the intriguing observations of anomalous diffusion of lipids and membrane proteins, we set out to develop a reasonably simple, but realistic enough numerical model to address properties of lipid membranes on the experimentally relevant spatial scales ( $\sim 1 \mu\text{m}$ ) and time scales ( $\sim 1 \text{ s}$ ). Results of such simulations can be directly confronted with experimental data obtained using optical microscopy-based methods typically used in membrane research (see, e.g., Figure 13 left).

The simulation approach we proposed in our works [11, 12] is based on the simplified lattice-based description of the membrane, which is assumed to consist of one or two lipids species on a square lattice (see Figure 13 right). (Similar simulations can also be carried out on lattices with a different geometry – we have recently found the equivalence conditions for simulations of this type on square and triangular lattices [13].) Each of the lipid species is represented by a collection of Ising spins in its own temperature-dependent external magnetic field (which is used to correctly represent the fluid-gel

transition of an individual membrane component). In case of a two-component membrane, these two Ising-type subsystems interact with each other. The system is thus not equivalent to the Ising model, but has been shown to be in the Ising universality class [14]. To be able to compare results of our simulations with the available experimental and simulation data, we chose the pair DMPC/DSPC as the composition and tuned the energetic parameters for lipids and their interaction to match this pair of lipids.

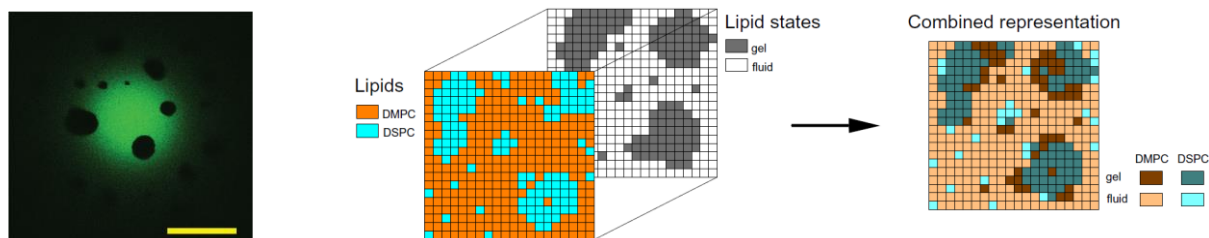


Figure 13: (left) Confocal fluorescence microscopy image of the upper pole of a GUV (DMPC/DSPC 50/50) exhibiting fluid–gel phase separation. Gel-phase domains, which coarsen and coalesce with time, appear on the image as dark areas. Scale bar: 20  $\mu\text{m}$ . (right) Square lattice model used in our work to simulate lipid membranes consisting of a mixture of two lipids (DMPC and DSPC in the present study). Individual lipid molecules occupy the nodes of a square lattice. Each of the two lipids (orange, cyan) can exist in either gel or fluid conformational state (black, white). The combined representation via four-colour coding makes it possible to see the complete configuration of the lattice in a single snapshot. (From Ref. [11]. Copyright © by IOP Publishing Ltd and Deutsche Physikalische Gesellschaft, 2011.)

As a result, we were able to accurately reproduce both the differential scanning calorimetry data and the corresponding phase diagram of this lipid system (Figure 14), which justified our choice of the numerical parameters of the model. The simulations, however, revealed that the calorimetry-based phase diagram gives only rather a rough picture, whereas a careful analysis of the spatial correlation functions and the structure factor of the membrane uncovered that the phase diagram has a critical point which is “hidden” by the way the calorimetry-based phase diagram is constructed (Figure 15). The presence of the critical point is confirmed by the expected behavior of the line tension, inverse correlation length, and inverse order parameter susceptibility vanish.

Away from the critical point in the gel-fluid coexistence regime, the model predicts the line tension of  $\sim 2$  pN, which is in a good agreement with the literature data for this lipid mixture. Upon an abrupt quench to the gel-fluid coexistence region, membrane domain growth follows a power-law with the exponent ranging from  $1/3$  to  $1/4$ , depending on the particular location on the phase diagram. The exponent, as well as the absolute rate of the domain growth, show a good agreement with the available experimental data.

We found that in the vicinity of the critical point, in presence of the near-critical fluctuations in the membrane, lipid molecules exhibit transient subdiffusion, which spans a few orders of magnitude in time, whereas away from the critical point diffusion is normal (Figure 16).

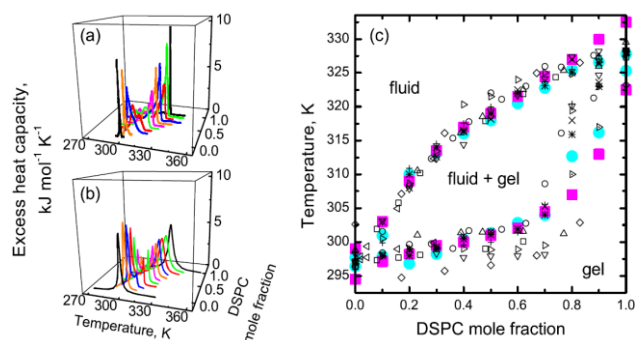


Figure 14: (a, b) Excess heat capacity curves for DMPC/DSPC lipid membranes for a range of compositions (DMPC/DSPC = 0/100, 10/90, 20/80, ..., 90/10, 100/0) measured experimentally by DSC (a) and obtained in our MC simulations (b). (c) Empirical phase diagram of DMPC/DSPC constructed from the excess heat capacity curves. Experimental (●) and MC simulation (■) data from our work in comparison with previously published experimental and simulation results – for details, see Ref. [11]. (From Ref. [11]. Copyright © by IOP Publishing Ltd and Deutsche Physikalische Gesellschaft, 2011.)

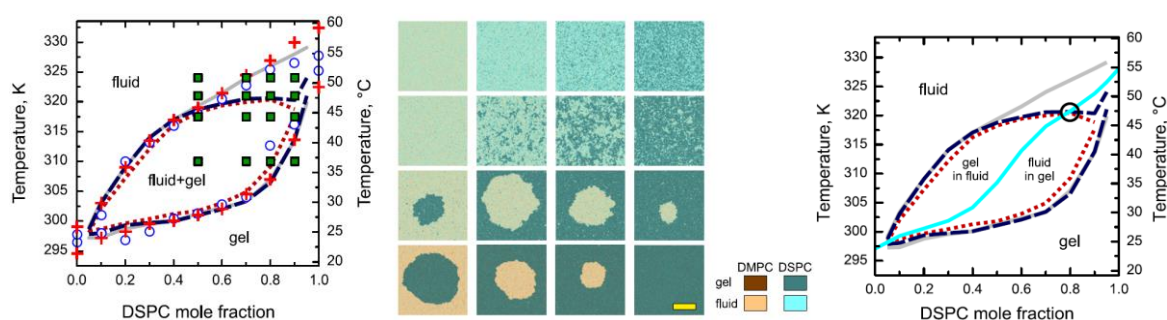


Figure 15: (left) phase diagram of the DMPC/DSPC lipid mixture. Empirical results obtained from the analysis of excess heat capacity curves from DSC measurements (○) and MC simulations (■). Lipid state spinodal (---), lipid state binodal (---) and lipid demixing curves (—) are shown – for details, see ref. [10]. Middle panel: membrane configurations corresponding to the compositions and temperatures marked by filled squares on the phase diagram. Lattice size: 600 × 600; scale bar: 200 lattice units ≈ 160 nm. (right) Phase diagram of the DMPC/DSPC system demonstrating the presence of a critical point. Lipid state spinodal, lipid state binodal, and lipid demixing curves are the same as in the left-hand side panel. The solid cyan line marks temperatures at which the DMPC/DSPC membrane shows equal amounts of the fluid and gel phase  $X_{\text{fluid}} = X_{\text{gel}} = 0.5$ . The critical point is marked with an open circle. (From Ref. [11]. Copyright © by IOP Publishing Ltd and Deutsche Physikalische Gesellschaft, 2011.)

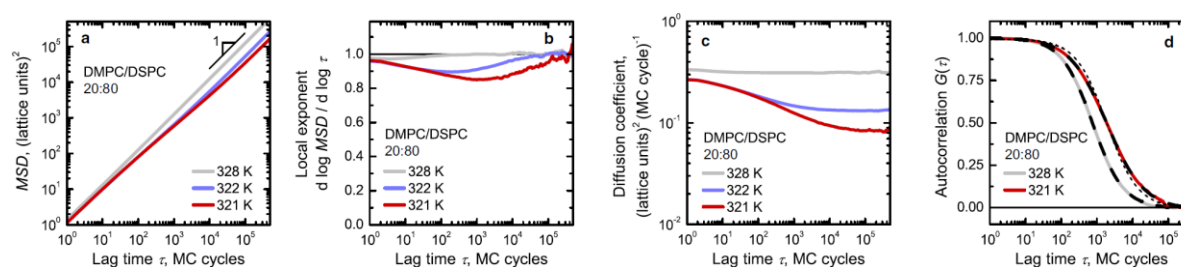


Figure 16: Effect of the proximity to the phase transition on diffusion of DMPC lipids in a DMPC/DSPC 20:80 membrane. Mean-square displacement  $MSD(\tau)$  (a), local exponent  $\beta_{MSD}(\tau)$  (b), time-dependent diffusion coefficient  $D(\tau)$  (c), and FCS autocorrelation  $G(\tau)/G(0)$  (d). (a–c) top to bottom:  $T = 328, 322,$  and  $321$  K. (d):  $T = 328$  (left) and  $321$  K (right). For clarity, data for 322 K are omitted in (d). (d) additionally shows fits to the FCS anomalous diffusion model giving the anomalous diffusion exponent  $\beta_{FCS} = 1.01$  at 328 K and  $\beta_{FCS} = 0.86$  at 321 K (---). For comparison, a fit of 321 K data with fixed  $\beta_{FCS} = 1.0$  is shown (- - -). (From Ref. [12]. Copyright © by The Biophysical Society, 2011.)

## 6 Effect of the membrane cytoskeleton on phase separation and diffusion in lipid membranes

In living cells, the plasma membrane tightly interacts with the cortical cytoskeleton which is anchored to the membrane via transmembrane proteins. As a result, one should expect that interaction with the cortical cytoskeleton can strongly affect both phase separation and the character of diffusion in the membrane. In our simulations [12], we represent a cytoskeleton using a Voronoi tessellation with a specified average mesh size (Figure 17 left). Additionally, we assume that the anchor proteins exert the aligning effect on the lipids, thus forcing them to assume the gel-phase conformation at the pinning site. The interaction of the membrane with the cytoskeleton has a striking effect on the phase separation character: The large-scale phase separation is strongly suppressed in the presence of the cytoskeleton (Figure 17 left). Furthermore, the dynamics of phase separation is also drastically changed: instead of a power-law growth characteristic of a free membrane, a very slow logarithmic growth is observed, typical for the random-field Ising model. This allowed us to suggest that the interaction with the cytoskeleton is the reason why micrometer-scale membrane domains are not observed in living cells. We also suggested that the cytoskeleton plays a cryoprotective role by delaying cold shock damage of living cell which is induced by large-scale phase separation.

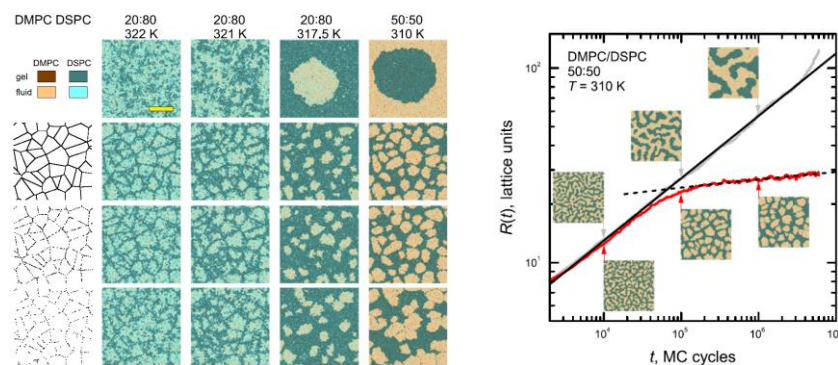


Figure 17: Effect of the membrane skeleton on the phase separation and domain coarsening in a DMPC/DSPC membrane. (left) Representative snapshots of membrane configurations are shown for the free membrane (first row), and membrane interacting with a network of filaments at 100 % (second row), 50 % (third row), and 25 % pinning density (fourth row). Snapshots for the free membrane, as well as for the membrane interacting with filaments at  $T = 321$  and  $322$  K, represent fully equilibrated configurations; snapshots for the membrane interacting with filaments at  $T = 310$  and  $317.5$  K correspond to equilibration time of  $6 \cdot 10^6$  MC cycles. For presentation purposes, the filaments are drawn thicker than they are in reality. Effect of the membrane skeleton on the domain growth in DMPC/DSPC 50:50 membrane abruptly cooled from the all-fluid state down to  $T = 310$  K in the fluid-gel phase coexistence region. Kinetics of domain growth when the membrane is free (upper curve) and in the presence of membrane skeleton with the filaments pinning density of 50 % (lower curve). (Solid line) Power law dependence  $R(t) \sim t^n$ , with  $n = 0.32$ ; (dashed line) stage of the slow logarithmic growth  $R(t) \sim \ln(t)$  in the presence of membrane skeleton. Representative membrane configurations obtained in our MC simulations at time instants  $10^4$ ,  $10^5$ , and  $10^6$  MC cycles are shown at the corresponding curves. Lattice size:  $400 \times 400$ ; scale bar: 125 lattice units  $\approx 100$  nm. (From Ref. [12]. Copyright © by The Biophysical Society, 2011.)

Our simulations [12] show that the presence of the cytoskeleton has also a pronounced effect on diffusion of lipids in the membrane. The effect is especially pronounced in the region of near-critical fluctuations of the free membrane. Specifically, an increase in the filament pinning density first enhances the anomalous diffusion and eventually leads to hop-diffusion of lipid molecules. The results on the

diffusion in the presence of the cytoskeleton are in a good qualitative agreement with the available experimental data from other groups.

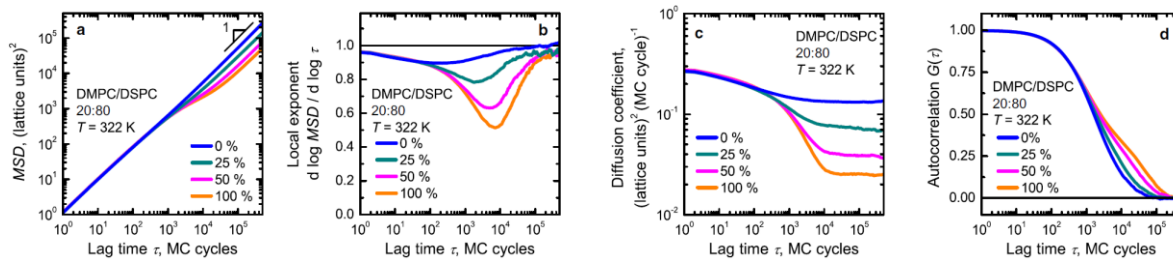


Figure 18: Effect of the membrane skeleton on diffusion of DMPC lipids in a DMPC/DSPC 20:80 membrane at 322 K. Mean-square displacement  $MSD(\tau)$  (a), local exponent  $\beta_{MSD}(\tau)$  (b), time-dependent diffusion coefficient  $D(\tau)$  (c), and FCS autocorrelation  $G(\tau)/G(0)$  (d). (a–c) top to bottom, and (d) left to right: filament pinning density equals 0 % (free membrane), 25 %, 50 %, and 100 %. (From Ref. [12]. Copyright © by The Biophysical Society, 2011.)

To verify the main conclusions based on our simulation work, we developed an experimental approach to study the effects of an artificial cytoskeleton on phase separation in multicomponent membranes using a minimalistic model system [15]. In this approach, we use GUVs composed of the quaternary lipid mixture DOPC/DOPG/eSM/Chol 2.5:2.5:3:2 as a mimic of a freestanding membrane which shows  $L_o$ – $L_d$  phase coexistence at temperatures below 37 °C (Figure 19 left). We employ a network formed of the GUV surface by the prokaryotic tubulin analog, FtsZ, as a minimal model of the membrane cytoskeleton (Figure 19 right). An artificial construct FtsZ-YFP-MTS is used for this purpose, where YFP is the yellow fluorescent protein which facilitates fluorescence microscopy observations, and MTS is the membrane targeting sequence derived from *E. coli* protein MinD.

The MTS inserts only into the outer leaflet of a bilayer and thus has a strong affinity to the  $L_d$  phase. Therefore, the MTS moieties attached to each of the monomer of the FtsZ polymeric network should act as nucleation centers for the  $L_d$  domains in the lipid membrane. Simultaneous imaging of the membrane and the attached FtsZ-YFP-MTS network at a range of temperatures below and above the transition temperature for phase coexistence shows that this is indeed the case (Figure 20).

We observe that coalescence of membrane domains at lower temperatures and melting of domains at higher temperatures is inhibited by the cytoskeleton – provided that the network is dense enough (typical mesh area  $< \sim 25 \mu\text{m}^2$ ). This serves as an argument in favor of the cryoprotective role of the cytoskeleton we put forward based on our simulations [12], and also suggests its protective role under hyperthermic conditions. For dense FtsZ networks, the domain sizes and shapes follow those of the meshes of the network (Figure 21A, B), whereas for large mesh sizes (mesh area  $> \sim 25 \mu\text{m}^2$ ) domains acquire rounded shapes and do not take up the whole mesh area (Figure 21C), which is a result of competition of wetting of filaments by the  $L_d$  phase and line tension at the  $L_o$ – $L_d$  interface. To additionally illustrate that the growth and coalescence of membrane domains are prevented by the cytoskeleton, we use protein MinC to disassemble the filament network on the membrane. Immediately upon removal of the FtsZ-YFP-MTS network from the membrane upon addition of MinC, the domains originally restricted by the FtsZ network start to move, grow, and coalesce to finally form considerably larger domains in a few minutes (Figure 21D).

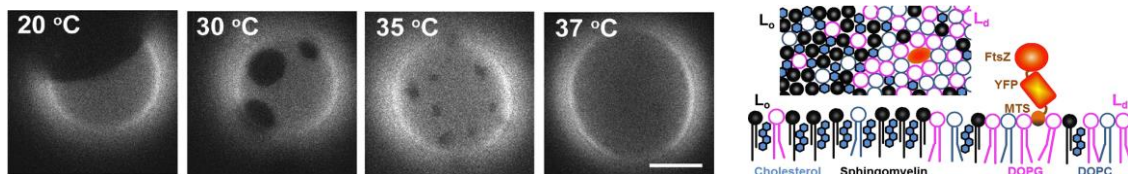


Figure 19: (left) GUVs composed of DOPC/DOPG/eSM/Chol 2.5:2.5:3:2 at various temperatures. At 37 °C, the membrane is homogeneous. (right) Schematic presenting the quaternary lipid system with FtsZ-YFP-MTS binding to the  $L_d$  phase. (From Ref. [15]. Copyright © by The Biophysical Society, 2015.)

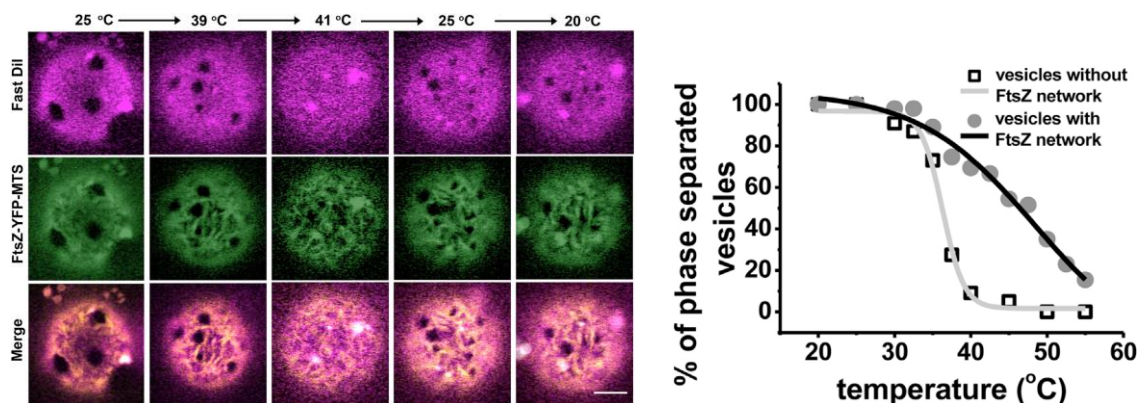


Figure 20: Effect of FtsZ meshwork on phase separation. Presence of dense FtsZ meshwork increases the phase transition temperature and inhibits growth of larger domains at temperatures much below phase transition temperatures. (left) Confocal fluorescence microscopy images of a GUV decorated with a dense FtsZ network. Note that the GUVs not immobilized and moves and reorients between the images corresponding to the different temperatures. Scale bar: 5  $\mu\text{m}$ . (right) Percentage of vesicles displaying phase separation in the presence and absence of FtsZ meshwork at different temperatures. Curves are drawn as a guide for the eye. (From Ref. [15]. Copyright © by The Biophysical Society, 2015.)

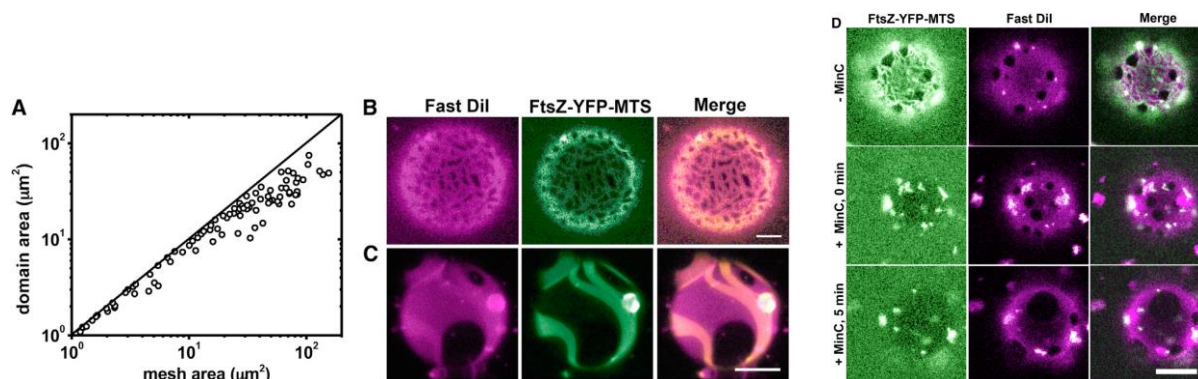


Figure 21: (A-C) Effect of the mesh size of the FtsZ network on the character of phase separation in the membrane. (A)  $L_o$  domain size as a function of the mesh size of the network formed by the FtsZ-YFP-MTS (symbols). The dependence  $y = x$  is shown as a guide for the eye (solid line). (B, C) Examples of the effect of dense (B) and sparse FtsZ network (C) on the domain sizes and shapes. (D) Effect of removal of the FtsZ filament network on phase separation in the membrane. (A) Confocal image of a pole of GUV showing assembled filaments as well as phase separation in the membrane. On addition of MinC ( $[\text{MinC}] = 1 \text{ mM}$ ,  $[\text{MinC}]/[\text{FtsZ}] \approx 1$ ), a depolymerase for FtsZ, the filaments are removed from the GUV, as seen by the absence of fluorescence on the GUV. Immediately after the removal of the FtsZ network, the domains become mobile, but their size is initially the same as in the presence of filaments. Mobile domains then start to coalesce and 5 min later, large domains are formed on naked GUVs. Temperature: 25 °C. Scale bars: 10  $\mu\text{m}$ . (From Ref. [15]. Copyright © by The Biophysical Society, 2015.)

We apply the minimalistic model approach in Monte Carlo simulations to demonstrate at the conceptual level that the cytoskeleton effect on phase separation is a very general phenomenon, whose main features do not depend on the molecular details of the system. To this end, we carry out lattice-based simulations for a binary lipid system. This time, we take into account the character of the interaction of the FtsZ-YFP-MTS network with the membrane, namely that the network pinning sites exert the disordering effect. Simulations for a range of temperatures for two different membrane compositions away from and close to a critical point (Figure 22) show that interaction with the cytoskeleton also in this case prevents large-scale phase separation when the system is cooled below the phase transition temperature. When the system is close to criticality, interaction with the cytoskeleton additionally preserves phase separation above the phase transition temperature. Thus, good qualitative agreement between simulations and experiment is observed.

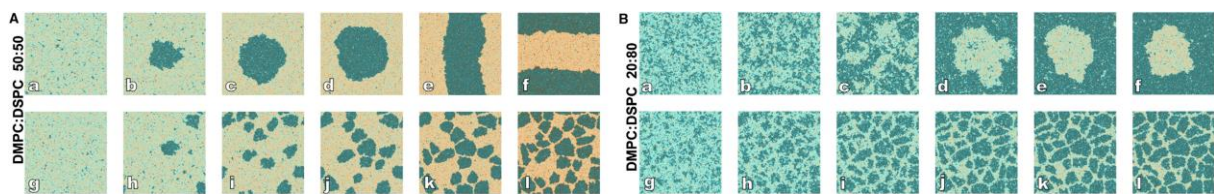


Figure 22: MC simulations of a two-component lipid membrane in the absence and presence of a membrane skeleton: (A) Effect of the cytoskeleton on the phase separation in the lipid membrane with the composition exhibiting an abrupt phase transition from the  $L_d$  (fluid) state to the  $L_d$ -solid ordered (fluid-gel) coexistence. The lipid composition is DMPC/DSPC 50:50. The corresponding transition temperature is  $T_t = 318.7$  K. Images (a–f) and (g–l) correspond to the free membrane and membrane interacting with the cytoskeleton, respectively. Simulations were carried out at the following temperatures:  $T = T_t$  (a, g),  $T = T_t - 1$  K (b, h),  $T = T_t - 3$  K (c, i),  $T = T_t - 5$  K (d, j),  $T = T_t - 9$  K (e, k), and  $T = T_t - 13$  K (f, l). (B) Effect of the cytoskeleton on the phase separation in the lipid membrane with the composition exhibiting a continuous phase transition from the  $L_d$  (fluid) state to the  $L_d$ -solid ordered (fluid-gel) coexistence via a critical point. The lipid composition is DMPC/DSPC 20:80. Transition temperature  $T_c = 320.5$  K. Images (a–f) and (g–l) correspond to the free membrane and membrane interacting with the cytoskeleton, respectively. Simulations were carried out at the following temperatures:  $T = T_c + 2$  K (a, g),  $T = T_c + 1$  K (b, h),  $T = T_c$  (c, i),  $T = T_c - 1$  K (d, j),  $T = T_c - 2$  K (e, k), and  $T = T_c - 3$  K (f, l). (From Ref. [15]. Copyright © by The Biophysical Society, 2015.)

## 7 Conclusion

Here, we reiterate the main findings of the works reviewed in this article:

- We have developed simple closed-form high accuracy approximations of the translational and rotational diffusion coefficients of membrane inclusions valid for arbitrary combinations of the inclusion size and viscosities of the membrane and surrounding fluids [1, 2].
- We demonstrated the successful application of these expression to determination of diffusion coefficients of membrane domains [1, 2], membrane-bound colloidal particles and DNA globules [6].
- We have demonstrated that spatially selective functionalization and fluorescent labeling of DNA origami nanoneedles can be used to provide their binding to lipid membranes, and allows for determination of their translational and rotational diffusion coefficients on the membrane using Fluorescence Correlation Spectroscopy [3].
- By studying translational and rotational diffusion of membrane-bound DNA nanoneedles as a function of their surface density by means of Fluorescence Correlation Spectroscopy and Monte Carlo simulations, we investigated the approach to the isotropic–nematic transition in a two-dimensional system of hard needle-like particles [4].

- We have developed an experimental method which allows one to reliably produce dome-shaped supergiant unilamellar vesicles containing cationic lipids by electroformation on ITO-coated electrodes, which provides an experimental platform for investigation of interactions of macromolecules and colloids with freestanding lipid membranes [5].
- We have discovered a new phenomenon of membrane-driven condensation of DNA molecules [6] and developed a theoretical model describing this phenomenon [8].
- We have developed a simplified lattice-based Monte Carlo approach which allows to simulate one- and two-component lipid membranes on experimentally relevant spatial scales and time intervals [11].
- We used this simulation approach to study processes of phase separation and diffusion in two-component lipid membranes [11, 12]; in particular, we found that Brownian motion of lipids in a two-component membrane shows transient anomalous diffusion in the vicinity of the critical point.
- We studied the effect of the membrane cytoskeleton on phase separation and diffusion in multicomponent lipid membranes using both computer simulations and experiments with a minimalistic system based on giant unilamellar vesicles and membrane-bound FtsZ protein network [12, 15]; we have found that the interaction with the cytoskeleton inhibits large-scale phase separation in multicomponent membranes, which offers explanation of the reason why micrometer-scale membrane domains are not observed in living cells and gives a molecular-level argument in favor of the cryoprotective role played by the membrane skeleton.

## Acknowledgements

The research reported in the manuscript has been supported by the Deutsche Forschungsgemeinschaft within project P5 “Diffusion and conformational dynamics in locally perturbed model membrane systems” of the Saxon Research Unit FOR 877 “From Local Constraints to Macroscopic Transport”.

## References

- [1] E.P. Petrov, P. Schwille: *Translational diffusion in lipid membranes beyond the Saffman–Delbrück approximation*. *Biophys. J.* **94**, L41–L43 (2008); *Correction*. *Biophys. J.* **103**, 375 (2012)
- [2] E.P. Petrov, R. Petrosyan, P. Schwille: *Translational and rotational diffusion of micrometer-sized solid domains in lipid membranes*. *Soft Matter* **8**, 7552–7555 (2012)
- [3] A. Czogalla, E.P. Petrov, D.J. Kauert, V. Uzunova, Y. Zhang, R. Seidel, P. Schwille: *Switchable domain partitioning and diffusion of DNA origami rods on membranes*. *Faraday Discuss.* **161**, 31–43 (2013); *Discussion*. *Faraday Discuss.* **161**, 113–150 (2013)
- [4] A. Czogalla, D.J. Kauert, R. Seidel, P. Schwille, E.P. Petrov: *DNA origami nanoneedles on freestanding lipid membranes as a tool to observe isotropic–nematic transition in two dimensions*. *Nano Lett.* **15**, 649–655 (2015)
- [5] C. Herold, G. Chwastek, P. Schwille, E.P. Petrov: *Efficient electroformation of supergiant unilamellar vesicles containing cationic lipids on ITO-coated electrodes*. *Langmuir* **28**, 5518–5521 (2012)
- [6] C. Herold, P. Schwille, E.P. Petrov: *DNA condensation at freestanding cationic lipid bilayers*. *Phys. Rev. Lett.* **104**, 148102 (2010)
- [7] C. Herold, P. Schwille, E.P. Petrov: *Single DNA molecules on freestanding and supported cationic lipid bilayers: Diverse conformational dynamics controlled by the local bilayer properties*. In preparation

- [8] A.G. Cherstvy, E.P. Petrov: *Modeling DNA condensation on freestanding cationic lipid membranes*. Phys. Chem. Chem. Phys. **16**, 2020–2037 (2014)
- [9] A.B. Artemieva: *MS Thesis*. TU Dresden (2013)
- [10] A.B. Artemieva, E.P. Petrov: *Interaction of semiflexible filamentous virus particles with freestanding lipid membranes*. In preparation
- [11] J. Ehrig, E.P. Petrov, P. Schwille: *Phase separation and near-critical fluctuations in two-component lipid membranes: Monte Carlo simulations on experimentally relevant scales*. New J. Phys. **13**, 045019 (2011)
- [12] J. Ehrig, E.P. Petrov, P. Schwille: *Cytoskeleton-assisted phase separation leads to subdiffusion in cell membranes*. Biophys. J. **100**, 80–89 (2011)
- [13] A.B. Artemieva, E.P. Petrov: *Lattice-based Monte Carlo simulations of lipid membranes: Correspondence between triangular and square lattices*. In preparation
- [14] C.-F. Lee, J. Ehrig, P. Schwille, E.P. Petrov: *Critical phenomenon in two-component membranes*. In preparation
- [15] S. Arumugam, E.P. Petrov, P. Schwille: *Cytoskeletal pinning controls phase separation in multicomponent lipid membranes*. Biophys. J. **108**, 1104–1113 (2015)